Mechanics of Advanced Materials and Structures, 9:257–272, 2002

1537-6494/02 $12.00 + .00
DOI: 10.1080/15376490290096955

Stress Redistribution in Skin/Flange Assemblies

KAREL MATOUŠ
GEORGE J. DVORAK

Department of Mechanical, Aerospace & Nuclear Engineering, Rensselaer Polytechnic Institute, Troy, New York, USA

ABSTRACT

A prestressing procedure is proposed for reduction of stress concentrations at the leading edges of adhesive bondlines in composite skin/flange assemblies. A finite-element analysis of a specific geometry of such an assembly is presented, which accounts for nonlinear viscoelastic deformation of the adhesive. Design diagrams based on elastic analysis are constructed for evaluation of prestress forces that reduce or completely eliminate adhesive stress concentrations caused by either tension stresses or bending applied to the skin.

Many composite structures contain skin/flange assemblies that provide attachment and support for stringers and other parts of the structure. Adhesive joints which are typically used in such applications are exposed to large stress concentrations at the leading edges of the bondline and the adjacent tapered end of the laminated flange. Joint failures often originate at these locations, as shown in numerous experiments by Kevin O'Brien's group at NASA-Langley [1, 2].

The present work shows that the stress concentrations contributing to such joint failures can be reduced or eliminated altogether by certain prestress forces applied to the skin/flange assembly prior to and then removed after adhesive cure. Prestress application can be accomplished by simple fixtures, as described in the first section. Since a stressed adhesive can undergo nonlinear viscoelastic deformation over time, we then discuss the relevant constitutive relations for the adhesive, and details of the finite-element analysis [3]. As expected, the nonlinear viscoelastic deformation is shown to reduce the adhesive stress concentrations. Next, a specific skin/flange assembly is selected and subjected to prestress followed by adhesive cure, prestress release, and subsequent mechanical loading by tension and bending applied to the skin. Design diagrams based on elastic analysis are constructed for evaluation of prestress forces that reduce or completely cancel adhesive stress components induced at the leading edges of the bondline by selected skin loads.

PRESTRESSED SKIN/FLANGE ASSEMBLY

Figure 1 shows a section of unit width b of a typical skin/flange geometry considered herein. Extending together with the skin in the x_2 direction, the flange serves to attach a

The authors appreciate financial support of this work by the Ship Structures and Systems S&T Division of the Office of Naval Research. Dr. Yapa D. S. Rajapakse served as program monitor. The authors would also like to acknowledge the CRC Press LLC, for permission to reproduce conference material.

Address correspondence to George J. Dvorak, 5012 JEC Rensselaer Polytechnic Institute, Troy, NY 12180-3590, USA. E-mail: dvorak@rpi.edu

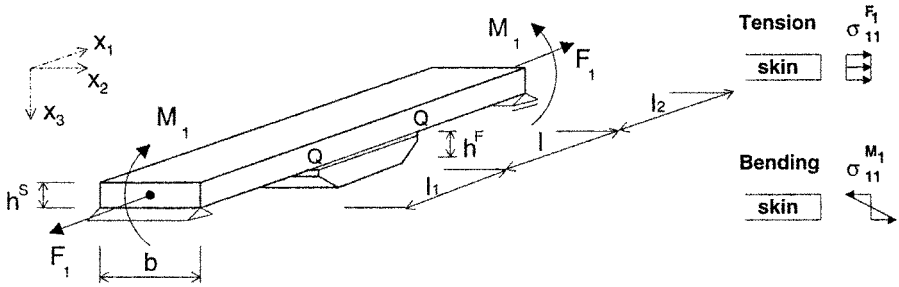

Figure 1. *Geometry of the skin/flange assembly.*

frame or a stiffener to the skin, say, of a bonded fuselage panel. Complex in-plane and out-of-plane loading of the panel is usually present in service; however, the load components that contribute most to local failure of the adhesive bond at flange ends are in-plane tension stress $\sigma_{11}^{F_1} = F_1/bh^S$, perpendicular to the leading edge of the flange, and transverse bending stress $\sigma_{11}^{M_1} = \pm 6M_1/b(h^S)^2$, applied to the skin outside the flange proper. These loads generate shear and peel stress concentrations at the ends (points Q) of the adhesive layer, making them preferred sites of adhesive failure or delamination at ply ends in a composite flange.

Our objective is to propose and analyze a controlled prestressing sequence applied during adhesive bonding of the flange, which introduces a favorable residual stress distribution at both ends of the bondline, and thus should enhance the load bearing capacity of the joint. Figure 2 outlines the proposed procedure. Immediately after application of the liquid adhesive at the bondline, the skin is loaded by a line force P applied at point S, while the flange is supported by a uniform compressive stress p at the tapered ends. In practice, this may be accomplished by supporting the flange ends by sealed liquid-filled pads. A small bending deflection in the positive direction of the x_3 axis is imparted to the assembly, and is maintained while the adhesive cures. After cure, all loads are removed. A certain part of the

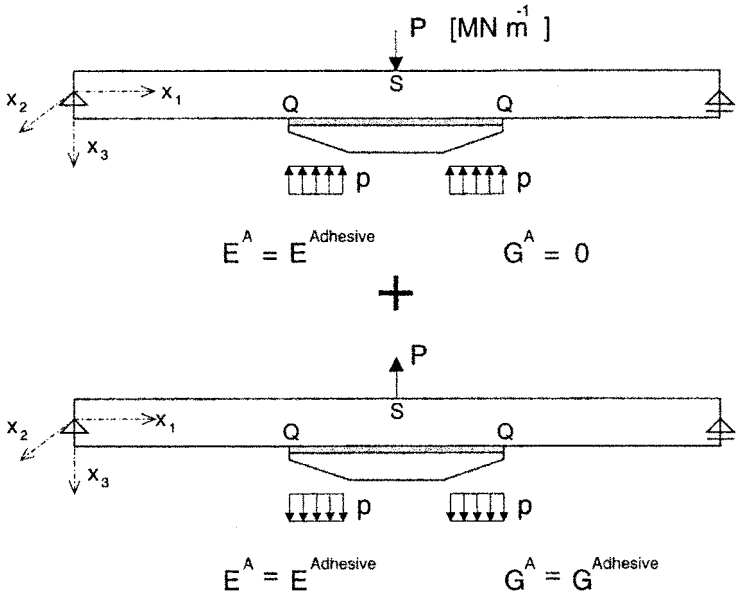

Figure 2. *Prestressing procedure.*

bending deflection is recovered, but another part is retained by the residual shear and peel stresses in the adhesive. It is probably obvious that the residual peel stress is compressive and the residual shear stress has an opposite sign to that generated by the tensile force F_1 and/or moment M_1.

The analysis that follows is concerned with evaluation of the adhesive stresses applied by the force F_1 and moment M_1, and of the adhesive residual stresses caused by release of the prestress force P. Results of the elastic solution are combined in design diagrams which allow selection of the prestress force such that the superimposed applied and residual stresses in the adhesive reach a selected minimum. Moreover, the effect of nonlinearly viscoelastic deformation of the adhesive on the local stress distribution is illustrated by several examples.

Analysis

The relatively complex geometry precludes reliable analytical evaluation of the stresses and deformations in the joint skin/flange assembly. Therefore, a two-dimensional finite-element solution has been used in the stress and deflection evaluations using the $Fem2D$ code, by Matouš [4]. A mesh consisting of three node elements based on linear shape functions was generated using the $T3D$ generator developed by Rypl [5]. A total of 8,737 nodes and 16,908 triangles were used in discretization of the domain. Six rows of elements were used to discretize the adhesive layer. Increased refinement to 100 rows of elements was used at the leading edges, to approximate the possibly singular stresses. Stress oscillations associated with the singularities were detected in very small volumes of the adhesive and adherends. These features depend on the fine-scale details of the local geometry that cannot be reliably reproduced in an actual structure. Therefore, thickness averages of the individual components were adopted in evaluation of the local stresses.

Both adherends were regarded as homogeneous, orthotropic elastic solids, with elastic constants equal to those of a woven composite laminate. A more refined analysis of a layered laminate would be needed in a specific application of the prestress technique. In development of the design diagrams that involved superposition of the residual and applied stress fields, the adhesive was assumed to be isotropic and elastic. Moreover, a nonlinearly viscoelastic adhesive was used in examples that illustrate prestress and stress relaxation.

The viscoelastic model adopted for the isotropic adhesive relies on the constitutive equation suggested by Schapery [6, 7],

$$\boldsymbol{\varepsilon}^t = g_0^{\boldsymbol{\sigma}\theta t}\boldsymbol{D}_0\boldsymbol{\sigma}^t + g_1^{\boldsymbol{\sigma}\theta t}\int_0^t \boldsymbol{J}^{(\psi^t-\psi^{\tilde{\tau}})}\frac{d}{d\tilde{\tau}}\left(g_2^{\boldsymbol{\sigma}\theta\tilde{\tau}}\boldsymbol{\sigma}^{\tilde{\tau}}\right)d\tilde{\tau} \qquad t\in\mathbb{R}^+ \tag{1}$$

where the superscripts $\boldsymbol{\sigma}, t, \theta$ refer to the value at current stress $\boldsymbol{\sigma}$, time $t \in \mathbb{R}^+$ and temperature θ, respectively. The symbol $\boldsymbol{D}_0$ denotes the elastic compliance tensor, $\boldsymbol{J}^t = D_c^{\psi^t}\bar{\boldsymbol{D}}$ is the creep compliance tensor, $D_c^{\psi^t}$ denotes a transient creep compliance function, and

$$\bar{\boldsymbol{D}} = \begin{bmatrix} 1 & -\nu^t & -\nu^t & 0 & 0 & 0 \\ & 1 & -\nu^t & 0 & 0 & 0 \\ & & 1 & 0 & 0 & 0 \\ & & & 2(1+\nu^t) & 0 & 0 \\ & & & & 2(1+\nu^t) & 0 \\ \text{sym.} & & & & & 2(1+\nu^t) \end{bmatrix} \tag{2}$$

Poisson's ratio ν^t can be generally time-dependent. Hence the present formulation is applicable to any thermorheologically simple isotropic viscoelastic adhesive. The $g_0^{\sigma\theta t}$, $g_1^{\sigma\theta t}$, $g_2^{\sigma\theta t}$ denote nonlinear kernel functions of stress $\boldsymbol{\sigma}$ and temperature θ in the time t. The function ψ^t is defined by

$$\psi^t = \int_0^t \frac{d\tilde{\tau}}{a^{\sigma\theta\tilde{\tau}}} \tag{3}$$

where $a^{\sigma\theta\tilde{\tau}}$ is a time-shift factor depending on the stress $\boldsymbol{\sigma}$ and temperature θ, respectively. The time-dependent strain in (1) thus depends on one function of time and four functions of stress and temperature. Specific evaluation of these functions appears in the Appendix, for the *FM*-73 adhesive characterized by Peretz and Weitsman [8].

As suggested by Henriksen [9] and Reddy and Roy [10, 11], the transient creep function can be expressed by the Prony series,

$$D_c^{\psi^t} = \sum_{r=1}^{N} D_r\left(1 - e^{-\lambda_r \psi^t}\right) \qquad \lambda_r = \frac{1}{\tau_r} \tag{4}$$

in which τ_r are constant retardation times and N denotes number of Prony coefficients $r \in \langle 1, N\rangle$. The values of D_r, which describe the strain increment during the time period τ_r, can be determined by fitting of the measured creep curves. The τ_r can be selected subject to certain well-known restrictions. Numerical studies confirmed that the retardation times can be chosen as $\tau_r = 10^{r-2}\tau_2$ for $r = 2, \ldots, N$, where τ_2 and N have to cover the time range of interest, and $\tau_1 \ll \tau_2$, e.g., $\tau_1 \approx 10^{-5}\tau_2$. The retardation spectrum plotted as $1/D_r$ versus τ_r ($r = 1, 2, \ldots, N$) fully characterize the material creep properties [12, 13].

Equation (1) can be expressed in a stress operator form,

$$\boldsymbol{\varepsilon}^t = \mathcal{F}(\boldsymbol{\sigma}^t) \tag{5}$$

where

$$\mathcal{F}(\boldsymbol{\sigma}^t) = \mathcal{J}^t \boldsymbol{\sigma}^t + \mathcal{E}^t \tag{6}$$

and the instantaneous compliance tensor $\mathcal{J}^t$ reads

$$\mathcal{J}^t = D_I^t \bar{\boldsymbol{D}} \qquad D_I^t = g_0^{\sigma\theta t} E^{-1} + g_1^{\sigma\theta t} g_2^{\sigma\theta t} \sum_r D_r\left(1 - \Gamma_r^t\right) \tag{7}$$

E is Young's modulus and Γ_r^t is the relaxation coefficient in the creep compliance series,

$$\Gamma_r^t = \frac{1 - e^{-\lambda_r \Delta\psi^t}}{\lambda_r \Delta\psi^t} \tag{8}$$

where

$$\Delta\psi^t = \int_{t-\Delta t}^{t} \frac{d\tilde{\tau}}{a^{\sigma\theta\tilde{\tau}}} \tag{9}$$

The hereditary strain component $\mathcal{E}^t$ is defined by

$$\mathcal{E}^t = \bar{\boldsymbol{D}} g_1^{\sigma\theta t} \sum_r D_r\left(g_2^{\sigma\theta(t-\Delta t)} \Gamma_r^t \boldsymbol{\sigma}^{t-\Delta t} - e^{-\lambda_r \Delta\psi^t} \boldsymbol{q}_r^{t-\Delta t}\right) \tag{10}$$

and the rth component, $q_r^{t-\Delta t}$, of the hereditary integral series at the end of the previous load step is

$$\boldsymbol{q}_r^{t-\Delta t} = \int_0^{t-\Delta t} e^{-\lambda_r(\psi^{t-\Delta t}-\psi^{\tilde{\tau}})} \frac{d}{d\tilde{\tau}}\left(g_2^{\sigma\theta\tilde{\tau}}\boldsymbol{\sigma}^{\tilde{\tau}}\right) d\tilde{\tau} \tag{11}$$

The hereditary integral at the end of the current step can be derived from the recurrence formula,

$$\boldsymbol{q}_r^t = e^{-\lambda_r \Delta\psi^t}\boldsymbol{q}_r^{t-\Delta t} + \left(g_2^{\sigma\theta t}\boldsymbol{\sigma}^t - g_2^{\sigma\theta(t-\Delta t)}\boldsymbol{\sigma}^{t-\Delta t}\right)\Gamma_r^t \tag{12}$$

where Γ_r^t is defined by Eq. (8). Once the strain vector (10) is known, the constitutive relation can be written as

$$\boldsymbol{\sigma}^t = \boldsymbol{L}^t(\boldsymbol{\varepsilon}^t - \mathcal{E}^t) \qquad \boldsymbol{L}^t = (\mathcal{J}^t)^{-1} \tag{13}$$

where $\boldsymbol{L}^t$ is the instantaneous stiffness tensor.

In the finite-element implementation of the above theory, the potential energy functional is based on (13),

$$\Pi = \frac{1}{2}\int_\Omega (\boldsymbol{\varepsilon}^t - \mathcal{E}^t)^T \boldsymbol{L}^t(\varepsilon^t - \mathcal{E}^t)\, d\Omega - \int_\Omega \boldsymbol{u}^T \bar{\boldsymbol{X}} d\Omega - \int_\Gamma \boldsymbol{u}^T \bar{\boldsymbol{p}}\, d\Gamma \tag{14}$$

After executing the partial derivative of Π with respect to the vector $\boldsymbol{u}^t$, and using standard isoparametric finite-element mapping, one obtains a system of algebraic equations,

$$\boldsymbol{K}^t\boldsymbol{d}^t = \boldsymbol{R}^t + \boldsymbol{R}_{\mathcal{E}}^t \tag{15}$$

where $\boldsymbol{K}^t$ is the symmetric, positive-definite global stiffness matrix after assembly and imposing the essential boundary conditions. The $\boldsymbol{d}^t$ denotes the global vector of free nodal parameters, and $\boldsymbol{R}^t$ is the vector of nodal forces due to externally applied mechanical loading and thermal effects. The load vector $\boldsymbol{R}_{\mathcal{E}}^t$ associated with the viscoelastic strain $\mathcal{E}^t$ is given by

$$\boldsymbol{R}_{\mathcal{E}}^t = \int_\Omega \boldsymbol{B}^T \boldsymbol{L}^t \mathcal{E}^t d\Omega \tag{16}$$

where $\boldsymbol{B}^T$ denotes strain displacement transformation operator. Note that in the nonlinearly viscoelastic case, the $\boldsymbol{K}^t$ contains embedded nonlinear material kernel functions $g_0^{\sigma\theta t}$, $g_1^{\sigma\theta t}$, $g_2^{\sigma\theta t}$ in the matrix $\boldsymbol{L}^t$.

A modified Newton-Raphson iteration technique was used to solve (15); the incremental displacement $\Delta\boldsymbol{d}_r^t$ obtained at the end of the rth iteration is used to update the local displacement for the nth time step,

$$\boldsymbol{d}_r^n = \boldsymbol{d}_{r-1}^n + \Delta\boldsymbol{d}_r^n \tag{17}$$

The iteration continues until convergence is achieved at each time step. The prestress initial condition $\boldsymbol{d}^0 = \boldsymbol{d}^{\text{prestress}}$ was used in the first time step.

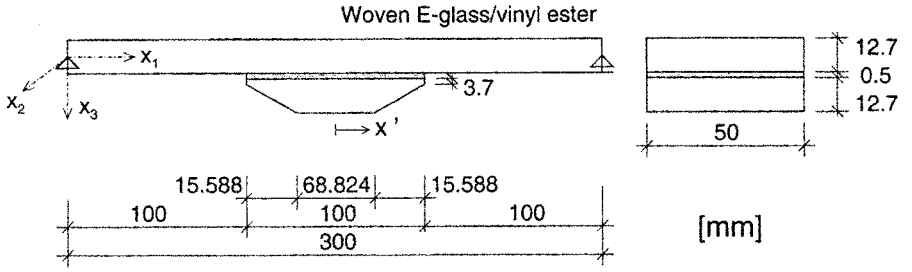

Figure 3. *The skin/flange configuration selected for stress analysis.*

Examples

1. Adhesive stresses after prestressing

As an illustration of the advantages of the prestressing concept, we analyzed the configuration shown in Figure 3, subjected to the loading sequence of Figure 2. Both skin and flange were regarded as homogeneous, orthotropic elastic solids, and the adhesive as a homogeneous isotropic solid with either elastic or nonlinearly viscoelastic response. Material selection was motivated by availability of material property data for the adhesive and adherends, Table 1. The viscoelastic properties of *FM*-73 adhesive are listed in the Appendix. No claim is made that the particular adhesive is suitable; in our related work [14], we found that the *Dexter-Hysol*; 9339 adhesive provided a strong bond of the adherend materials. However, no time-dependent property data were found for this particular adhesive.

Shown first are stress distributions in the elastic adhesive, which should be good approximations of short-time response. The specific applied load magnitudes were selected with regard to the estimated allowable stresses in the adherends. Figure 4 describes the adhesive stress components before and after prestress release, Figure 2, in the absence of any external loads. In the first part of the prestressing sequence shown in the top half of Figure 2, the adhesive is liquid and thus capable of transmitting only compressive normal stress between skin and flange. This σ_{33} component, shown in Figure 4, has local maxima at flange ends and at the center section, and stress is supported by the adhesive at the end of adhesive cure. Additional stresses that may be caused by the curing process were not considered in the absence of relevant material data.

Prestress release is represented by the loads in the bottom drawing of Figure 2, which are now applied to the bonded structure. Significant stress changes are now observed in the cured adhesive layer, Figure 4. In addition to a different peel stress σ_{33}, the adhesive now supports a shear stress σ_{31} and a longitudinal normal stress σ_{11}. The peel stress remains compressive, and the shear stress sign is opposite to that caused by the subsequent tension applied to the skin. The σ_{11} has very small effect on joint failure.

Table 1
*Elastic moduli of the adherends and adhesive [*GPa*]*

Material	E_1	E_3	G_{31}	ν
Woven E-glass/vinyl ester	22.00	8.90	3.17	0.38
FM-73 adhesive	2.778	2.778	1.006	0.38

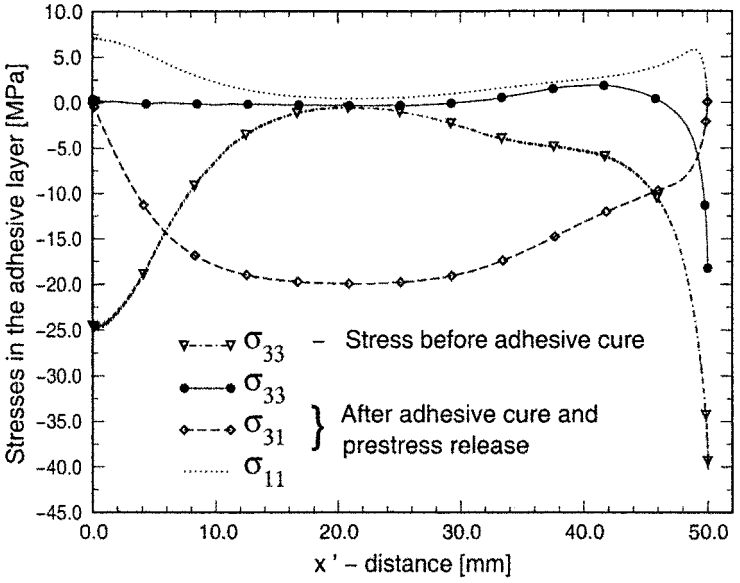

Figure 4. *Adhesive stresses before and after prestress release,* x = *0.36* NM/m.

2. Adhesive stresses due to prestress and skin tension

Figure 5 shows the adhesive stresses caused by skin tension stress $\sigma_{11}^{F_1} = 90$ MPa, applied in the absence of prestress. As expected in this adhesive joint configuration, there are large tensile peel stress and shear stress concentrations at the leading edge of the flange. Numerical values are listed in the second column of Table 2.

Superposition of the adhesive stresses due to prestress and skin tension is presented in Figure 6; the maxima are listed in the third elastic column of Table 2. These results

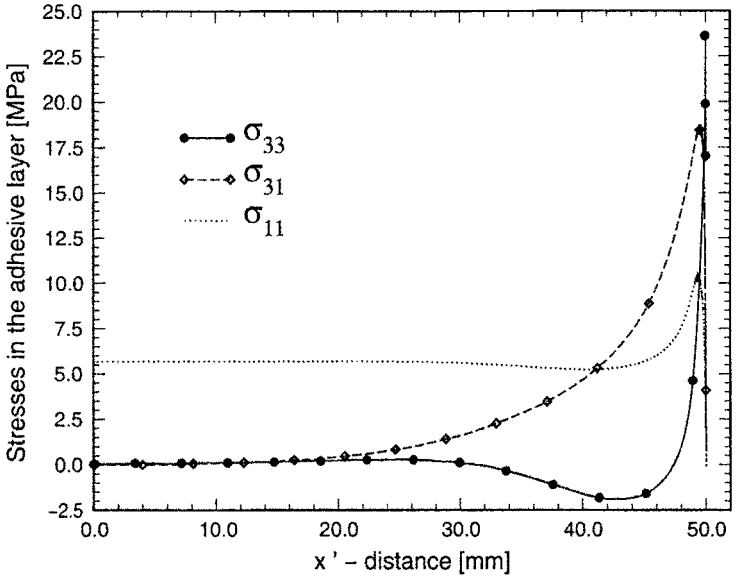

Figure 5. *Stresses induced in the adhesive by tension stress* $\sigma_{11}^{F_1} = 90$ MPa.

Table 2
Adhesive stress maxima caused by different tensile loading histories [MPa]

	Tension without prestress	Tension after prestress		
Stress	Elastic	Elastic	Nonlinear 24-h	Nonlinear 48-h
σ_{33}	23.59	4.05	2.66	1.61
σ_{31}	18.54	14.87	13.61	12.35
σ_{11}	10.40	15.95	13.93	12.65

clearly demonstrate the very large reduction of the adhesive peel stress in the prestressed joint, in the elastic case by a factor of 5.82. The shear stress maximum is also reduced, and so are both components by the nonlinear viscoelastic deformation after 24 or 48 h, Table 2. The very small peel stress value at the leading edge of the bondline also implies reduced likelihood of ply delamination in the tapered end of the flange, and also in the skin.

The stresses obtained in the elastic analysis can be scaled and used to construct a design diagram for selection of the prestress force needed to counteract the effect of the applied skin tension stress, Figure 7. The maxima of the adhesive stress components are plotted as linear functions of the transverse tension stress $\sigma_{11}^{F_1}$ in the top half of the Figure 7. The bottom half contains plots of the local stress maxima as functions of the prestress force P applied prior and during adhesive cure. For example, for $\sigma_{11}^{F_1} = 30$ MPa, we draw the horizontal line $A_1 \rightarrow A_2 \rightarrow A_3$ to find the respective stress component maxima in the skin/flange structure without prestress. If zero peel stress is desired under the prescribed transverse tension in the prestressed structure, we draw the vertical line $A_3 \downarrow B_3$, to intercept with the σ_{33} line in the lower half of the figure. Proceeding now horizontally along $B_3 \rightarrow B_2 \rightarrow B_1$, we find

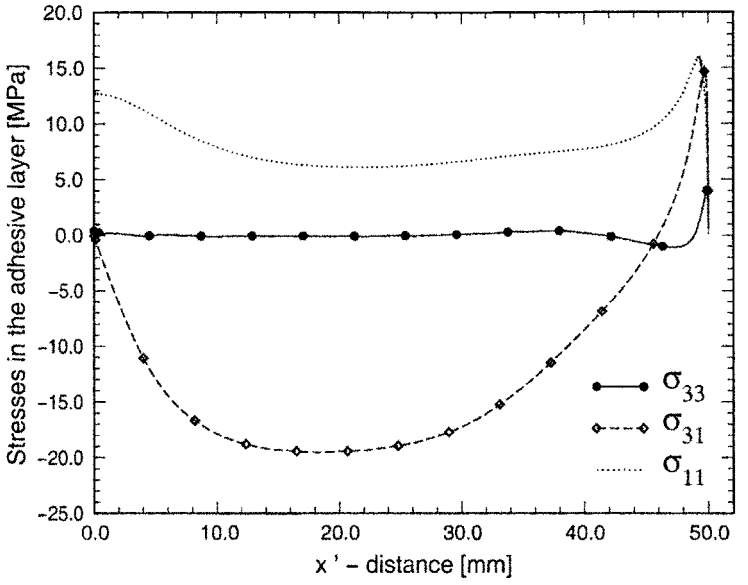

Figure 6. *Stresses in the adhesive after superposition of prestress and skin tension contributions from Figures 4 and 5.*

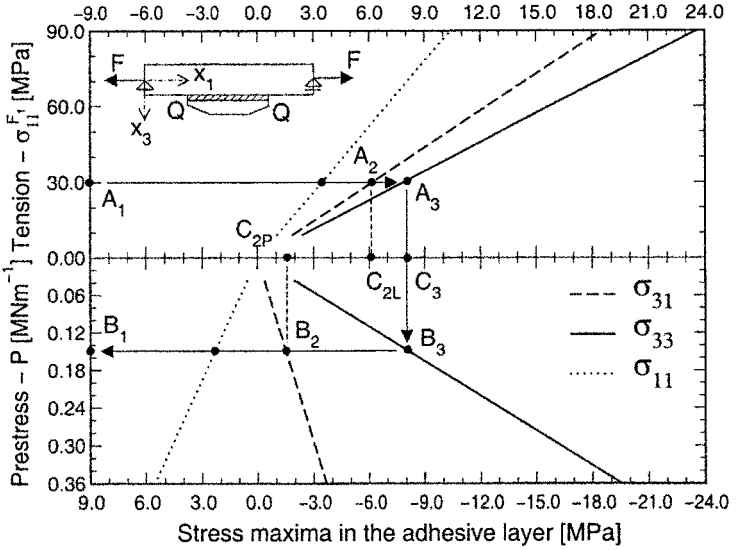

Figure 7. *Prestress design diagram for the skin/flange assembly subjected to skin tension.*

the required prestress force $P = 0.15$ MN/m. The maximum shear stress is obtained by subtracting the values of σ_{31} at point C_{2L} from that at C_{2P}. In the present case, $\sigma_{31}\ (C_{2L}) - \sigma_{31}\ (C_{2P}) = 4.4$ MPa.

Next, to illustrate the effect of nonlinear viscoelastic deformation in the adhesive, we selected the loading history shown in Figure 8. The joint of Figure 3 was prestressed by the same force $P = 0.36$ MN/m, and this force was removed after adhesive cure. A 24-hr relaxation period was allowed before application of the skin tension stress $\sigma_{11}^{F_1} = 90$ MPa, which was then kept at a constant level for the next 24 h. The stress changes occurring in the adhesive during these two 24 h intervals were monitored, as shown for the σ_{33} component in Figure 9. The stress relaxation rates tend to zero before the end of each interval. Figures 10–12 display the stress distributions found in the adhesive layer after there specified time intervals. These represent changes in the initial elastic distributions of Figure 6; the stress maxima are also listed for easy comparison in Table 2. As expected, all stresses are reduced. The largest difference, from $\sigma_{33} = 4.05$ MPa to $\sigma_{33} = 1.61$ MPa is found in the peel stress, but this is a additional reduction from the elastic value of 23.59 MPa in the absence of prestress.

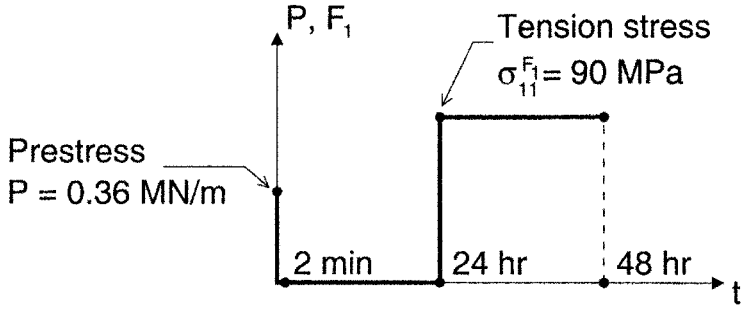

Figure 8. *The prestress and skin tension loading history applied in nonlinear viscoelastic analysis of the adhesive.*

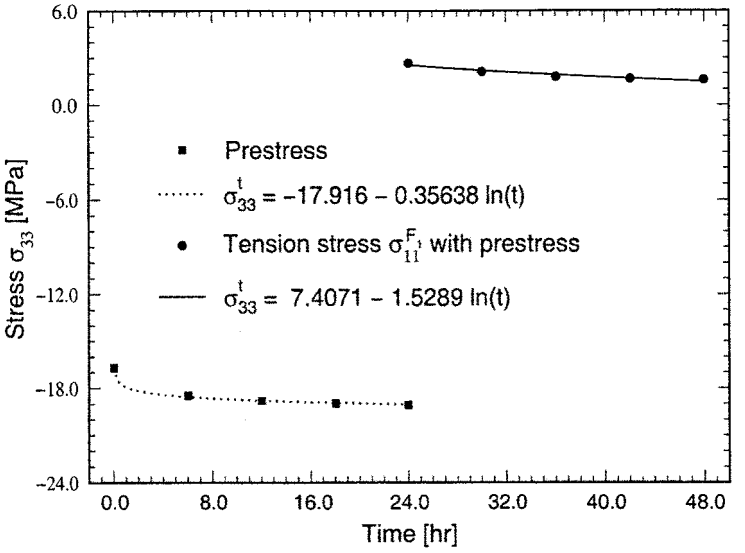

Figure 9. *Time distribution of stress σ_{33} at different stages of the loading history of Figure 8.*

Figure 13 presents the vertical deflection of the structure along the length of the flange. If zero deflections are imposed at the far ends of the skin, the tension stress of $\sigma_{11}^{F_1} = 90$ MPa causes the midsection to rise by 1.3 mm. The prestress force causes a downward deflection of 6.0 mm, which is reduced to about 4.4 mm by prestress release and further to 3.0 mm after the 48-h loading sequence shown in Figure 8. These illustrative values suggest that the residual deflection is of the same order of magnitude as that imposed by the transverse tension stress. However, the difference in sign appears to be improve structural integrity, as it promotes compression in the bondline between the skin and the frame or stringer that may be attached to the flange.

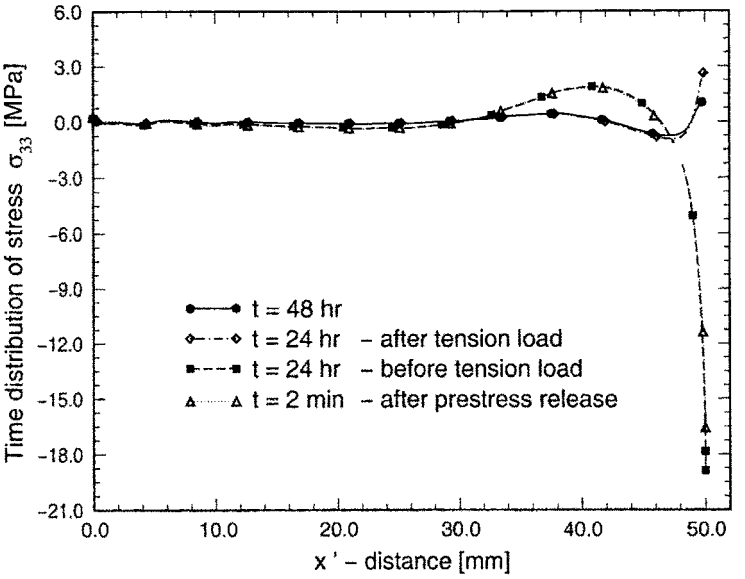

Figure 10. *Adhesive peel stress σ_{33} at different stages of the loading history of Figure 8.*

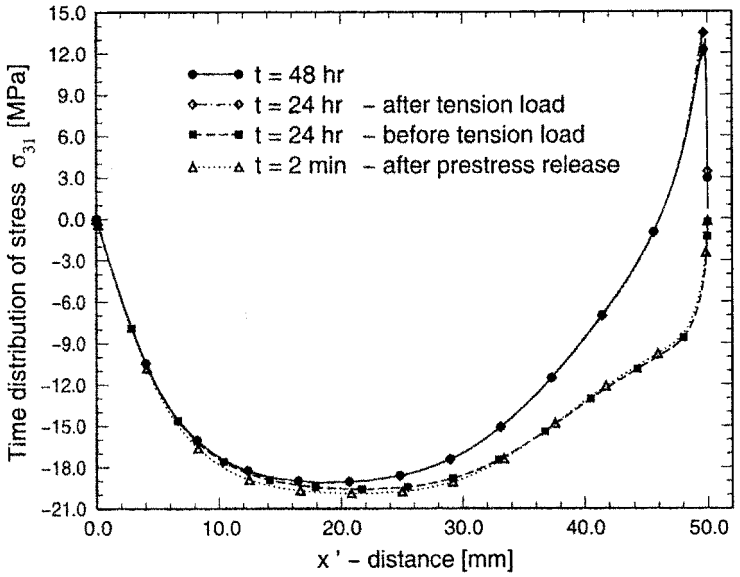

Figure 11. *Adhesive shear stress σ_{31} at different stages of the loading history of Figure 8.*

3. Adhesive stresses due to prestress and skin bending

In addition to the tension stress, the skin may also be subjected to bending moments, as shown in Figure 1. The moment sign may change or oscillate, but of interest here is the moment direction that exposes the bottom layer of the skin and the flange to tensile stress $\sigma_{11}^{M_1}$. The opposite moment direction would actually return the structure to a configuration similar to that under prestress, with compressive peel stress and favorable shear stress distribution in the adhesive. Since we have already established the beneficial effect of viscoelastic deformation of the adhesive, we present only the elastic stress distributions and a design diagram.

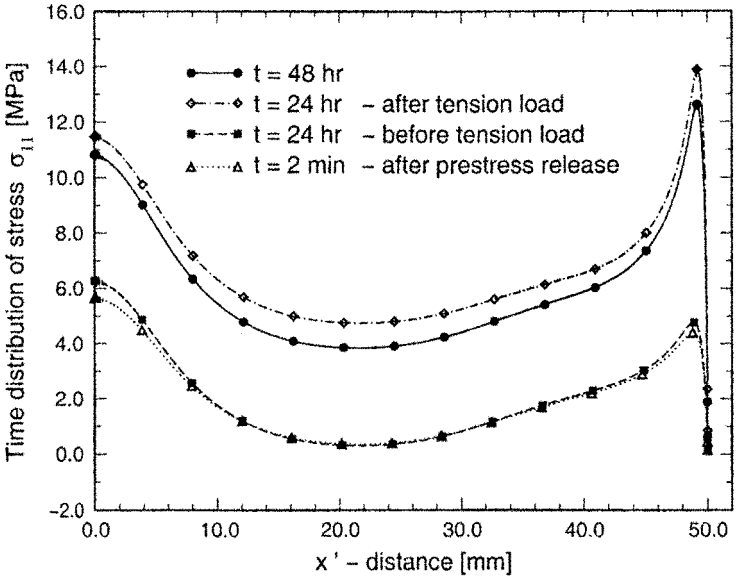

Figure 12. *Adhesive normal stress σ_{11} at different stages of the loading history of Figure 8.*

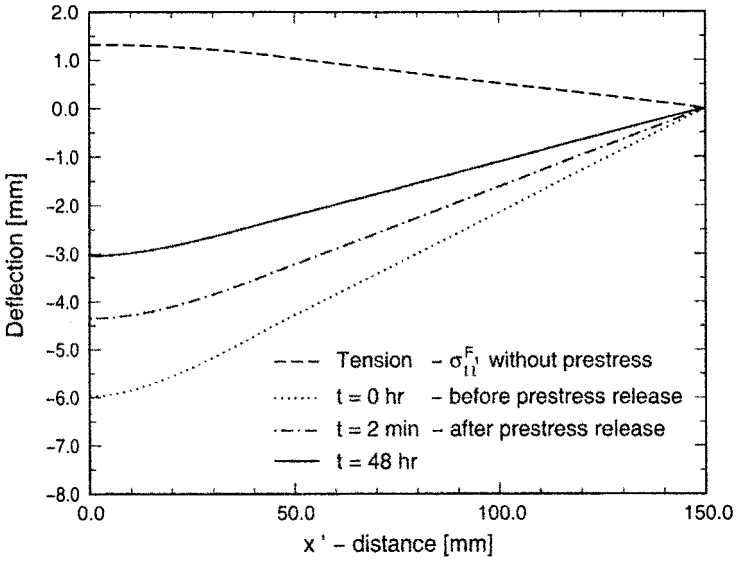

Figure 13. *Deflection of the skin under skin tension and after the loading sequence of Figure 8.*

The starting point here is again the stress distribution in the adhesive after prestress release, Figure 4. The effect of the bending moment on adhesive stresses was evaluated in the bonded skin/flange assembly, under $M = 1.075 \times 10^{-3}$ MNm/m, which caused the tensile stress $\sigma_{11}^{M_1} = \pm 40$ MPa in the free skin. Deformation of the bottom skin layer, indicated by the tensile stress rather than the moment value itself, should have a decisive effect on the adhesive stresses. These stresses are shown in Figure 14. The maximum peel

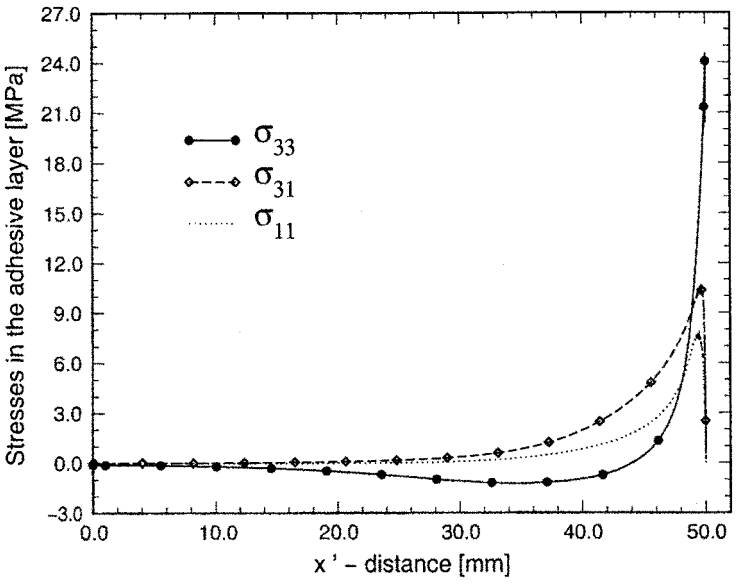

Figure 14. *Stresses induced in the adhesive by bending stress* $\sigma_{11}^{M_1} = \pm 40$ MPa *applied to the skin.*

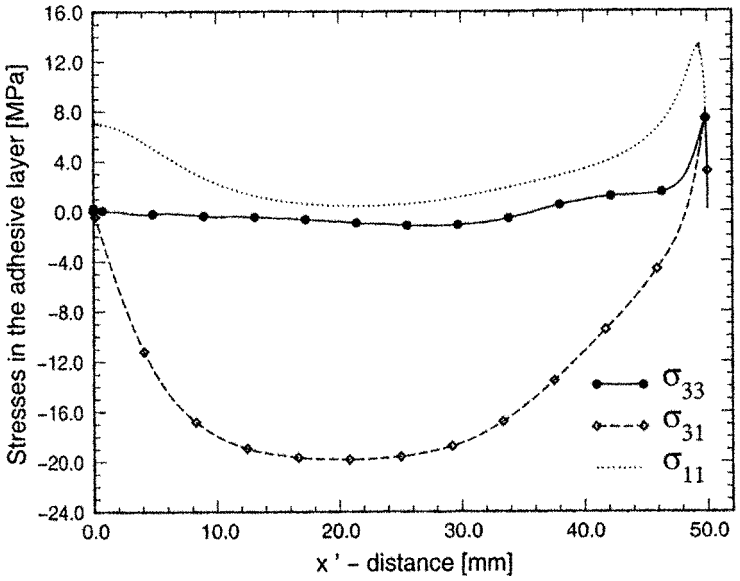

Figure 15. *Stresses in the adhesive after superposition of prestress and bending moment contributions from Figures 4 and 14.*

stress value is similar to that caused by the skin tension, but the shear and normal stresses exhibit lower maxima. Superposition of the stresses in Figure 14 with those caused by the original prestress in Figure 4 is presented in Figure 15. Stress maxima are compared in Table 3. A design diagram indicating the desired prestress for a selected maximum value of the bending-induced tensile stress is constructed in Figure 16. The design sequence starts again at point A_1, which corresponds to the selected bending stress $\sigma_{11}^{M_1}$. The design path is then analogous to that followed in the design diagram for tension load, Figure 7.

Since both design diagrams in Figures 7 and 16 are based on elastic stress analysis, they can be used jointly in finding the prestress needed to counteract the effect of superimposed tension and bending. Such prestress force could be found by simply adding the forces found to reduce the expected maxima of the two loading components. If the assembly were loaded by skin compression and tension-inducing bending, or vice versa, the design diagrams could be easily adopted for loading by reverse bending and/or skin compression. In such an application, the top stress branches in these figures could be extended as straight lines into the negative tension or bending stress regions, and the bottom stress branches into the negative prestress regions, implying prestressing in a direction opposite to that shown

Table 3
Adhesive stress maxima caused by different bending loading histories [MPa]

	Bending without prestress	Bending after prestress
Stress	Elastic	Elastic
σ_{33}	24.56	7.37
σ_{31}	10.43	7.42
σ_{11}	7.73	13.25

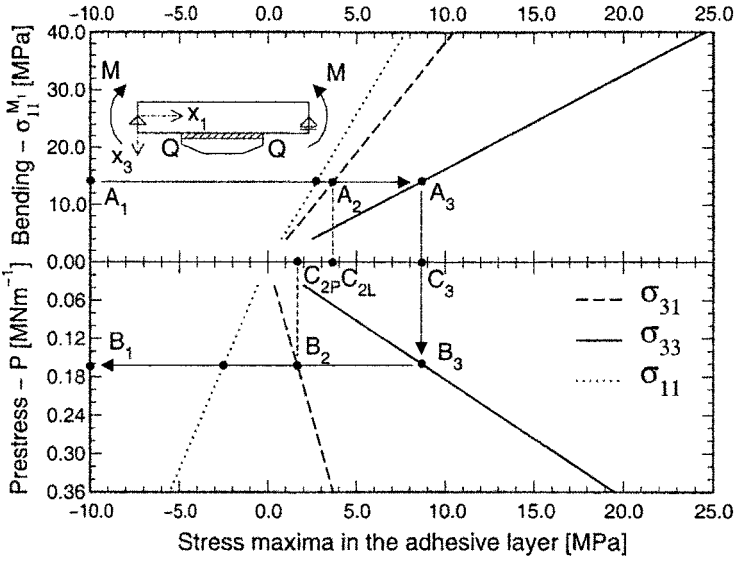

Figure 16. *Prestress design diagram for the skin/flange assembly subjected to the bending.*

in Figure 2. The prestress magnitude needed for the combined loading can then be found by superimposing the values found for each of the two loading components. Moreover, since the top parts of the diagrams show the stress maxima caused by the respective loading components, they could also be used to determine, for example, how much skin compression is needed to counteract the effect of bending, or vice versa, without the benefit of prestress.

Conclusion

The results suggest a relatively simple method of adhesive stress reduction in a skin/flange assembly loaded either by skin tension and/or bending, acting transverse to the longitudinal axis of the flange. While certain special fixtures would be required for prestressing, the expected enhancement of load-bearing capacity and/or endurance may well be worth the extra cost. The present numerical study should be also confirmed by experimental strain measurement techniques for adhesive bonds, such as Moiré interferometry.

Possible viscoelastic deformation of the adhesive tends to reduce over time the stress maxima at the leading edges of the flange bondline. Therefore, design diagrams based on elastic stress analysis should suffice, and lead to conservative designs in most applications. This would also obviate the need for a detailed evaluation of the material parameters required in the nonlinear adhesive analysis. Since the adhesive stress distributions depend on both adhesive and adherend elastic moduli and details of the joint geometry, construction of the design diagrams should be based on a finite-element evaluation of the stress distributions. Scaling of solutions obtained for a single load magnitude is permissible in the elastic case.

In an actual composite structure, both flange and skin are made of a laminate consisting of several fibrous layers. Layup details may influence the adhesive stresses at the leading edge of the bondline, and also the interlaminar stresses at the tapered free edges of the laminated flange. Indeed, failure of the joint often originates in the tapered flange end, and extends along ply interfaces before reaching the adhesive layer [1, 2]. Since the laminates were homogenized in our analysis, the results do not reflect that level of detail. However, inasmuch as the goal was to minimize the stress concentrations at the bondline leading edge by superposition of the prestress and applied loading stress distributions, the differences

between the layered and homogenized solutions should not have a large effect on the loading combinations found to generate the minimized stress distributions.

References

[1] J. Li, T. K. O'Brien, and C. Q. Rousseau, *J. Am. Helicopter Soc.*, vol. 42, no. 4, pp. 350–357, 1997.

[2] M. K. Cvitkovich, T. K. O'Brien, and P. J. Minguet, Fatigue Debonding Characterization in Composite Skin/Stringer Configurations, in R. B. Bucinell (ed.), *Composite Materials: Fatigue and Fractures* (ASTM STP 1330), vol. 7, pp. 97–121, 1998.

[3] T. J. R. Hughes, *The Finite Element Method: Linear Static and Dynamic Finite Element Analysis*, Prentice-Hall, Englewood Cliffe, NJ, 1987.

[4] K. Matouš, Analysis and Optimization of Composite Materials and Structures, Ph.D. thesis, *CTU Reports*, vol. 4, no. 3/2000, Prague, Czech Republic, 2000.

[5] D. Rypl, Sequential and Parallel Generation of Unstructured 3D Meshes, Ph.D. thesis, *CTU Reports*, vol. 2, no. 3/1998, Prague, Czech Republic, 1998.

[6] R. A. Schapery, A Method of Viscoelastic Stress Analysis Using Elastic Solutions, *J. Franklin Inst.*, vol. 279, pp. 268–289, 1965.

[7] R. A. Schapery, On the Characterization of Non-linear Viscoelastic Materials, *Polym. Eng. Sci.*, vol. 9, no. 4, pp. 295–310, 1969.

[8] D. Peretz and Y. Weitsman, Nonlinear Viscoelastic Characterization of FM-73 Adhesive, *J. Rheology*, vol. 26, no. 3, pp. 245–261, 1982.

[9] M. Henriksen, Nonlinear Viscoelastic Stress Analysis—A Finite Element Approach, Comput. Struct., vol. 18, no. 1, pp. 133–139, 1984.

[10] S. Roy and J. N. Reddy, Finite-Element Models of Viscoelasticity and Diffusion in Adhesively Bonded Joints, *Int. J. Num. Meth. Eng.*, vol. 26, pp. 2531–2546, 1988.

[11] J. N. Reddy and S. Roy, Finite-Element Analysis of Adhesive Joints, in L. H. Lee (ed.), *Adhesive Bonding*, pp. 359–394, Plenum Press, New York, 1991.

[12] Z. P. Bažant and S. Prasannan, Solidification Theory for Concrete Creep. II: Verification and Application, *J. Eng. Mech.*, vol. 115, no. 8, pp. 1704–1725, 1989.

[13] Z. P. Bažant and Y. Xi, Continuous Retardation Spectrum for Solidification Theory of Concrete Creep, *J. Eng. Mech.*, vol. 121, no. 2, pp. 281–287, 1995.

[14] G. J. Dvorak, J. Zhang, and O. Canyurt, Adhesive Tongue and Groove Joints for Thick Composite Laminates, *Composites Sci. Technol.*, vol. 61, pp. 1123–1147, 2001.

Appendix

Nonlinear viscoelastic characterization of the FM-73 adhesive

Here we describe viscoelastic material properties of the *FM*-73 adhesive obtained by Peretz and Weitsman [8]. The viscoelastic behavior of this adhesive can be completely characterized by the compliance function $D_c^{\psi^t}$ shown in Figure 17, representing the strain ε^t of adhesive at time t. Poisson's ratio is assumed constant for this adhesive. The nonlinear effects for the constant temperature $\theta = 303$ K are expressed by means of stress-dependent material kernel functions,

$$g_0^{\sigma\theta t} = 1 + 0.2\left(\frac{\tilde{\sigma}^t}{\sigma_{\text{ult}}}\right) \tag{18}$$

$$g_1^{\sigma\theta t} = 1 + 1.435\left(\frac{\tilde{\sigma}^t}{\sigma_{\text{ult}}}\right)^{2.4} \tag{19}$$

$$g_2^{\sigma\theta t} = 1 + 0.75\left(\frac{\tilde{\sigma}^t}{\sigma_{\text{ult}}}\right)^{2.0} \tag{20}$$

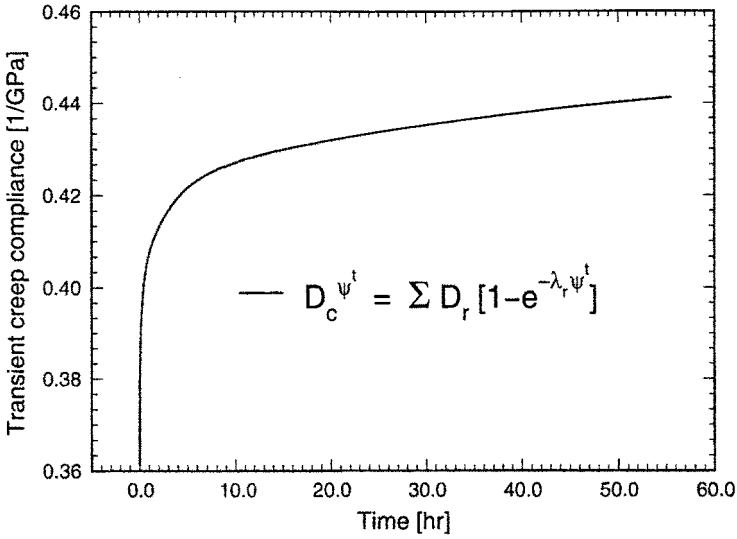

Figure 17. *The transient creep compliance* $D_c^{\psi^t}$.

where the ultimate stress $\sigma_{\text{ult}} = 50$ MPa and equivalent Mises stress $\tilde{\sigma}^t = \sqrt{\frac{3}{2} s_{ij} s_{ij}}$. The shift factor $a^{\sigma\theta t}$ is given by

$$a^{\sigma\theta t} = e^{\frac{-1.5\tilde{\sigma}^t}{\sigma_{\text{ult}}}} \tag{21}$$